An antiparallel cell circulation driven by self-alignment induces phase separation

Ryunosuke Karimata[1], Hidenori Hashimura[2], Shuhei A. Horiguchi[3], Taihei Fujimori[2,4], Satoshi Sawai[2,5], Satoru Okuda[3, 6*]

[1] Division of Nano Life Science, Graduate School of Frontier Science Initiative, Kanazawa University, Kanazawa 920-1192, Japan

[2] Graduate School of Arts and Sciences, The University of Tokyo, Tokyo 153-8902, Japan

[3] Nano Life Science Institute, Kanazawa University, Kanazawa 920-1192, Japan

[4] Chan Zuckerberg Biohub, San Francisco, CA 94158, USA

[5] Research Center for Complex Systems Biology, Universal Biology Institute, The University of Tokyo, 3-8-1 Komaba, Meguro-ku, Tokyo 153-8902, Japan

[6] Sapiens Life Sciences, Evolution and Medicine Research Center, Kanazawa University, Kanazawa 920-8640, Japan

*** Corresponding author: satokuda@staff.kanazawa-u.ac.jp**

ABSTRACT

Cell sorting is a form of phase separation in populations of motile cells, such as epithelia. Cell polarity often plays a central role in cell sorting by influencing motility, adhesion, and mechanical stress. However, whether and how self-alignment of individual cells—without direct polarity coordination—can lead to stable domain formation remains unclear. Here, we introduce "circulation-induced phase separation" (CirPS)—a distinct mechanism of phase separation driven by hierarchical cell ordering. Each polar motile cell, which self-aligns its polarity with its velocity, migrates by generating a tension gradient along its polarity at cell–cell boundaries, rather than by traction on the substrate. Two-dimensional (2D) vertex model simulations of a mixture of polar motile and nonmotile cells reveal phase separation of stable motile cell domains, each consisting of concentric cell circulations, with adjacent circulations aligned in an antiparallel direction. Domain formation proceeds in a self-enforcing manner: circulations generate a normal stress difference that effectively attracts the motile cells themselves, driving domain growth. Cell speed increases with the degree of ordering, and the domain size grows over time following a $1/3$ power-law scaling in the low-noise

regime—features distinct from conventional sorting, such as motility-induced phase separation and the Vicsek model. A similar antiparallel circulation pattern was observed in 2D aggregates of *Dictyostelium discoideum,* supporting the biological relevance of CirPS.

I. INTRODUCTION

Phase separation occurs across diverse natural systems, including biological cells [1–3]. Specifically, heterogenous constituents in mixtures can separate due to variations in interactions and properties, such as differences in adhesion, size [4–8], and mass [9,10]. Additionally, phase separation can be driven by active behaviors, including differences in contraction [11], motility [12,13], diffusivity [14], chirality [15], or nematic stress activity [16–18]. These mechanisms are relevant to biological behaviors, particularly cell sorting in densely packed tissues such as epithelia [2,19–24], which play key roles in processes including embryogenesis and carcinogenesis [3,16,25–27]. Motility-induced phase separation (MIPS) is a well-established mechanism in active matter systems [28–32], where self-propelled particles aggregate due to reduced motility. However, this mechanism is mainly effective in dilute or semi-dilute conditions. In densely packed tissues, where cells are tightly connected and spatially constrained, alternative or additional mechanisms are likely to contribute to phase separation in these compact environments.

Motile biological cells with cell-intrinsic polarity often form stable aggregates [33–36]. Zebrafish lateral line cells and breast cancer cells are well-known examples where polar motile cells form clusters and exhibit collective migration [37–40]. From a theoretical point of view, this type of phase separation—most well-known in the Vicsek model—has been attributed to the “mutual alignment” or “polarity-polarity alignment” mechanism, which assumes direct coordination of polarity between neighboring cells. Such a mechanism typically leads to the formation of unidirectionally polarized clusters [41–43] and, with additional modifications, can produce vortices [44–46]. However, it remains unclear how cells explicitly acquire polarity information from their neighbors or, indeed, whether such direct information transfer actually occurs in biological systems.

Alternatively, sorting in compacted-cell systems may arise solely through intracellular control, wherein each cell aligns its polarity to its own velocity—a process known as “self-alignment” or “polarity-velocity alignment.” Previous studies demonstrated that self-alignment can indeed induce cell flocking, characterized by collective motion with local polarity order [40,47–50]. However, flocking does not necessarily imply phase separation, and whether self-alignment alone can support phase separation remains largely unexplored. One exception is a specific case in which nonmotile cells aggregate due to interactions with surrounding polar motile cells [47]. Recent work in dense tissues shows that flocking can arise from either mutual or self-alignment mechanisms [51].

Nonetheless, earlier studies suggest that these mechanisms may differ in their capacity to drive phase separation. Thus, elucidating whether self-alignment can drive phase separation—and, if so, whether it exhibits features distinct from those arising from mutual alignment—is of central importance for understanding the mechanisms of cell sorting of polar motile cells.

In addition to alignment mechanisms, the nature of forces that drive cell movements may have a major bearing on cell sorting. In tightly adhered cells, there are two primary sources of force. One is traction on the substrate, in which a self-propelled force directly drives individual cells forward [37–40]. The other is a tension gradient at cell–cell boundaries, where adjacent cells are used as a scaffold to drive migration [42,52–57]. Cell-substrate traction combined with self-alignment has been reported to induce phase separation-like cell behaviors [47]. However, under these conditions, it is nonmotile cells rather than motile cells that form aggregates. Moreover, how these behaviors arise remains poorly understood. In contrast, a junctional tension gradient is observed in actual migrating cells, such as Walker-256 carcinosarcoma cells, which migrate by utilizing polarized actin localization and cortical actin flow [52]. Such processes have also been studied theoretically [42,52,57]. However, their interaction with self-alignment remains unexplored. Thus, examining the tension gradient-driven motility is essential for determining whether and how self-alignment leads to the formation of stable motile cell domains.

In this study, we performed numerical simulations of mixtures of polar motile and nonmotile cells using a two-dimensional (2D) vertex model. The model assumes that each motile cell possesses a dynamic polarity that favors alignment with its own velocity. Along this polarity, a tension gradient is generated at the boundaries between adjacent cells. Our results demonstrate that self-alignment induces phase separation of motile cells into stable domains surrounded by nonmotile cells. Remarkably, within each domain, motile cells align to form a closed-loop circulation, with adjacent circulations aligning in antiparallel directions. This arrangement induces a normal stress difference that drives phase separation. Moreover, we found a similar antiparallel circulation pattern in aggregating *Dictyostelium discoideum*, showing the relevance of this phenomenon in biological systems. Collectively, our findings uncover a distinct mechanism of phase separation driven by self-alignment and resulting cell circulations, setting it apart from conventional phase separation mechanisms.

II. MODEL

The multicellular dynamics are described using a 2D vertex model [58–61]. A cell monolayer is represented as a polygonal tiling, where each polygon corresponds to a cell, and vertices and edges are shared among adjacent cells [Fig. 1(a)]. Cell rearrangements through T1 transitions occur when

the length of an edge becomes smaller than the threshold length Δl [Fig. 1(b)]. The system box is defined on an *xy*-plane within $0 < x < L_x$ and $0 < y < L_y$, with periodic boundary conditions imposed at $x = 0, L_x$ and $y = 0, L_y$. The box is filled by N_c cells, consisting of N_m motile-type cells indexed by $\mathcal{M} \coloneqq \{1,2,\cdots,N_\mathrm{m}\}$ and $N_\mathrm{n} \coloneqq N_\mathrm{c} - N_\mathrm{m}$ nonmotile-type cells indexed by $\mathcal{N} \coloneqq \{N_\mathrm{m}+1,\cdots,N_\mathrm{c}\}$ [Fig. 1(a)]. The mixing ratio of motile-type and nonmotile-type cells is given by $\phi \coloneqq N_\mathrm{m}/N_\mathrm{c}$.

The system is characterized by the positions of N_v vertices, denoted as $\{\boldsymbol{r}_i\}_{i\in\{1,\cdots,N_\mathrm{v}\}}$, and the orientation of the polarity of N_m motile-type cells, denoted by $\{\theta_\alpha\}_{\alpha\in\mathcal{M}}$. The polarity of the α-th cell is also expressed as a normalized vector $\boldsymbol{q}_\alpha = (\cos\theta_\alpha,\ \sin\theta_\alpha)$. Note that $\boldsymbol{q}_\alpha$ is defined for motile-type cells but not for nonmotile-type cells.

The time evolution of $\{\boldsymbol{r}_i\}$ follows overdamped dynamics, described by

$$\eta\frac{\mathrm{d}\boldsymbol{r}_i}{\mathrm{d}t} = -\frac{\partial U}{\partial \boldsymbol{r}_i}. \tag{1}$$

The left-hand side in Eq. (1) describes the friction force with the coefficient η, and the right-hand side describes the mechanical force derived from the effective energy U. Cell behaviors are described by a standard energy function widely used in previous studies [59,60,62], given by

$$U = \sum_{\alpha=1}^{N_\mathrm{c}}\left[\frac{K_\mathrm{A}}{2}(A_\alpha - A_0)^2 + \frac{K_\mathrm{P}}{2}(P_\alpha - P_0)^2 + \sum_{\varepsilon\in\mathcal{E}_\alpha}\gamma_{\alpha\varepsilon}l_\varepsilon\right]. \tag{2}$$

The first term on the right-hand side in Eq. (2) expresses the area elastic energy, where K_A is the area elasticity modulus, A_α is the area of the α-th cell, and A_0 is the preferred cell area. The second term expresses the perimeter elastic energy corresponding to the perimeter contraction by actomyosin rings and cell–cell adhesion by adhesion molecules, where K_P is the perimeter elasticity modulus, P_α is the perimeter of the α-th cell, and P_0 is the preferred perimeter of cells. The third term expresses the tension energy acting on edges, where $\gamma_{\alpha\varepsilon}$ is the tension on the ε-th edge of the α-th cell, l_ε is the length of the ε-th edge, and $\mathcal{E}_\alpha$ is the set of edges that compose the α-th cell.

Our model assumes that each motile-type cell generates a driving force by establishing a junctional tension gradient along its edges, with the direction of the gradient aligned with the polarity of the cell, as suggested by previous studies [42,52,57]. The tension $\gamma_{\alpha\varepsilon}$ for $\varepsilon \in \mathcal{E}_\alpha$ is expressed as

$$\gamma_{\alpha\varepsilon} = \begin{cases} -\gamma^\mathrm{p}\cos\varphi_{\alpha\varepsilon} & (\alpha\in\mathcal{M}) \\ 0 & (\alpha\in\mathcal{N}) \end{cases}. \tag{3}$$

Here, γ^p represents the strength of polarized tension, and $\varphi_{\alpha\varepsilon}$ denotes the angle between the polarity vector $\boldsymbol{q}_\alpha$ and the vector from the center of the α-th cell to the midpoint of the ε-th edge [Fig. 1(c)]. From Eq. (3), each motile-type cell moves within the packed cell population in the direction of its

polarity by generating positive tension on the rear side and negative tension on the front side. Although the tension $\gamma_{\alpha\varepsilon}$ inherently depends on $\{\boldsymbol{r}_i\}$ and $\{\theta_\alpha\}$ through $\varphi_{\alpha\varepsilon}$, we assume that $\gamma_{\alpha\varepsilon}$ is determined autonomously by cellular activities. Thus, $\gamma_{\alpha\varepsilon}$ is treated as a constant when calculating the force using Eq. (1); i.e., $\partial\gamma_{\alpha\varepsilon}/\partial\boldsymbol{r}_i = 0$. This assumption renders the tension gradient to act as an active force, breaking the detailed balance.

We next introduce the dynamics of $\{\boldsymbol{q}_\alpha\}$ for the motile-type cells. Here, we assume self-alignment, meaning that the polarity of each cell aligns with the orientation of its velocity [36,38,49,63–68]. Additionally, accounting for rotational diffusion caused by noise, the time evolution of $\boldsymbol{q}_\alpha$ $(= (\cos\theta_\alpha,\ \sin\theta_\alpha))$ is described by

$$\frac{\mathrm{d}\theta_\alpha}{\mathrm{d}t} = J\sin(\psi_\alpha - \theta_\alpha) + w_\alpha, \tag{4}$$

where J is the alignment rate and ψ_α is the orientation of the centroid velocity of the α-th cell. Additionally, w_α represents white Gaussian noise, satisfying $\langle w_\alpha(t)\rangle = 0$ and $\langle w_\alpha(t)w_{\alpha'}(t')\rangle = 2D_r\delta_{\alpha\alpha'}\delta(t-t')$, where D_r is the noise intensity. From Eq. (4), the characteristic time scale on which polarity aligns with velocity is determined by J and D_r [Fig. 1(d)].

All parameters are nondimensionalized by the unit length $\sqrt{A_0}$, unit time $\eta/(K_\mathrm{A}A_0)$, and unit energy $K_\mathrm{A}{A_0}^2$. The parameters $K_\mathrm{p} = 1$, $\gamma^\mathrm{p} = 0.20$, $N_\mathrm{c} = 32 \times 32$, and $\phi = 0.50$ are fixed in all simulations, unless otherwise specified, while J and D_r are varied. To ensure that varying the values of J and D_r does not affect the tissue fluidity, the nondimensionalized preferred perimeter $p_0 \coloneqq P_0/\sqrt{A_0}$, known as the target shape index, is fixed at $p_0 = 3.90$, meaning that the system remains in a fluid-like state [69] (see Appendix A). Equations (1) and (4) are solved numerically using the Euler method from $t = 0$ to $t = T = 10^4$ with a time step of $\Delta t = 0.01$. The threshold length of T1 transitions is set to $\Delta l = 0.05$.

III. RESULTS

A. Self-alignment and the tension gradient induce a phase separation with motile cell domains

First, to quantitatively evaluate whether the system exhibits phase separation, we introduced the separation degree μ as an order parameter

$$\mu \coloneqq 1 - \frac{1}{\phi}\left(\frac{1}{N_\mathrm{n}}\sum_{\alpha\in\mathcal{N}}\frac{n_\alpha^\mathrm{m}}{n_\alpha^\mathrm{m} + n_\alpha^\mathrm{n}}\right), \tag{5}$$

where n_α^m and n_α^n are the numbers of motile-type and nonmotile-type cells adjoining the α-th cell, respectively. $\mu \approx 1$ indicates phase separation, while $\mu \approx 0$ indicates a homogeneous system.

By varying J and D_r, we found that the cells underwent phase separation when $J > D_r$: motile-type cells spontaneously cohered and formed domains surrounded by nonmotile-type cells [Fig. 2(a) and Movie S1]. During phase separation, the value of μ increased and then plateaued, whereas μ remained near zero when no phase separation occurred [Fig. 2(b)]. Furthermore, the plateau value of μ was close to unity for larger J and smaller D_r values [Fig. 2(c)]. When $J < D_r$, phase separation did not occur; even when a pre-separated structure was used as the initial condition, the system reverted to a disordered configuration (see Appendix B). Notably, phase separation occurred even at $D_r = 0$ when $J \neq 0$. Conversely, phase separation did not occur when $J = 0$ and $D_r \neq 0$, indicating that self-alignment is essential for phase separation [Fig. 2(c)]. Moreover, we found a steep transition of μ with respect to J for small D_r values, revealing a critical point, whereas the transition became more gradual as D_r increased [Fig. 2(d)]. These results indicate that the phase separation is driven by cell polarity and the active force and thus is distinct from thermal phase separation.

B. Ordering leads to dynamic scaling with 1/3 power-law domain growth

To investigate the macroscopic behavior of the observed phase separation, we analyzed several quantities, including the mean-square displacement (MSD) of motile-type cells and the time evolution of the domain size [Fig. 3(a)] (see Appendix C for detailed methods). For short timescales, cells show ballistic behavior because $\mathrm{MSD} \propto \tau^2$. For longer time scales, the MSD scales because $\mathrm{MSD} \propto \tau^\lambda$ ($\lambda < 1$) for large J values, indicating subdiffusive motion under full phase separation. In contrast, for small J values, the MSD exhibits normal diffusion, as $\mathrm{MSD} \propto \tau^1$, due to the dominance of noise. These observations suggest that motile-type cells display the subdiffusive behavior typical of phase separation. Moreover, in the parameter range where phase separation occurs, the domain size increases proportionally to the $1/3$ power of time when phase separation is complete, that is, when the alignment rate is moderate ($J \lesssim 7$) and noise is low ($D_r \lesssim 1$); otherwise the domain size increases proportionally to the 1/4 power of time [Figs. 3(b) and 3(c)]. Across the 1/3 and 1/4 regimes, spatial correlations at different time points collapse onto a single curve that signifies a scaling function, with distances rescaled by the corresponding domain size $R(t)$ [Fig. 3(d)]. This finding indicates that the system exhibits dynamic scaling, evolving self-similarly over time through coarsening dynamics governed by a single characteristic growing length scale of the domain structure [70].

Our model exhibits a growth exponent of $\nu = 1/3$ in the domain growth law $R \propto t^\nu$ within the low-noise regime. The same exponent is known in MIPS that is induced by run-and-tumble motion [31,71]. In contrast, $\nu = 1/4$ is typically observed in MIPS, which is induced by active

Brownian motion [31,72,73], and in the standard Vicsek model [74,75]. The difference in the growth exponent suggests a difference in how domain growth is driven. The exponent $\nu = 1/4$ is typically attributed to direct domain coalescence via diffusion-coalescence processes [76–79], although the exact mechanisms underlying domain growth in the Vicsek model remain subject to debate. However, the exponent $\nu = 1/3$ is characteristic of diffusion-limited dynamics [24,80,81], indicating that diffusion is the primary driver of domain coarsening.

C. An antiparallel circulation pattern emerges within a motile cell domain

We next examined the cell movement and polarity dynamics with respect to the domains that formed under phase separation conditions. We found that motile-type cells form a vortex-like pattern [Fig. 4(a) and Movies S2, S3] (see Appendix D for detailed methods). The pattern is characterized by a concentric alignment of the velocity and polarity. Furthermore, cells sharing the same velocity and polarity direction align in a chain-like arrangement, which we shall refer to as "circulation." These circulations are organized in concentric onion-like layers, with adjacent circulations aligned and moving in antiparallel directions [Fig. 4(b)].

To quantify the emergence of antiparallel alignments in each cluster, we introduced pairwise order S as an order parameter

$$S := \frac{1}{N_{\mathrm{m}}} \sum_{\alpha \in \mathcal{M}} \left[\frac{1}{n_{\alpha}^{\mathrm{m}}} \sum_{\alpha' \in \mathcal{M}_{\alpha}} \chi_{\alpha\alpha'} \mathrm{sgn}(\boldsymbol{q}_{\alpha} \cdot \boldsymbol{q}_{\alpha'}) \right], \tag{6}$$

where $\mathcal{M}_{\alpha}$ represents the set of motile-type cells adjoining the α-th motile-type cell. The term $\chi_{\alpha\alpha'}$ is defined as

$$\chi_{\alpha\alpha'} := \begin{cases} -1 & -\frac{\sqrt{3}}{2} < \frac{(\boldsymbol{r}_{\alpha'} - \boldsymbol{r}_{\alpha}) \cdot \boldsymbol{q}_{\alpha}}{\|\boldsymbol{r}_{\alpha'} - \boldsymbol{r}_{\alpha}\|} < \frac{\sqrt{3}}{2}, \\ 1 & \text{otherwise} \end{cases} \tag{7}$$

where $\boldsymbol{r}_{\alpha}$ represents the centroid of the α-th motile-type cell. When the α'-th cell centroid lies within a $\pi/3$ cone forward or backward relative to $\boldsymbol{q}_{\alpha}$, $\chi_{\alpha\alpha'} = 1$; otherwise $\chi_{\alpha\alpha'} = -1$ [Fig. 4(c)]. $S \approx 1$ indicates that each domain is predominantly filled with antiparallel alignments, whereas $S \approx 0$ indicates random polarity. By averaging S over the time interval $t = 0.95T$ to $t = T$, we confirmed that phase separation is accompanied by the emergence of antiparallel alignment [Fig. 4(d)]. Notably, this alignment and the resulting phases emerged stably under low-noise conditions, whereas they appeared only transiently or did not appear under higher-noise conditions.

Moreover, to analyze cell dynamics during phase separation, we quantified the average speed of motile-type cells and found that their speed increased over time when phase separation occurred [Fig. 4(e)], whereas it remained constant without phase separation [Fig. 4(f)]. This result suggests that the mechanism of phase separation observed here is fundamentally different from MIPS, in which particles aggregate due to a reduction in speed caused by repeated collisions and deceleration [31].

D. Cell circulation induces a normal stress difference to drive phase separation

To address how cell circulation leads to phase separation, we calculated the stress tensor of each cell (see Appendix E). The result shows that a normal stress difference emerges within a domain [Figs. 5(a)–5(c)], i.e., the tensile principal stress direction of each cell aligns the circumferential direction within the domain, while the compressive direction aligns the radial direction. Moreover, we found that hydrostatic pressure is larger within the domain than in the surrounding nonmotile-type cells [Fig. 5(d)]. These results show that cell circulation produces a normal stress difference to wring cells themselves. A normal stress difference induces stress-dependent deformation in viscoelastic materials, as seen in the Weissenberg effect [82]. This mechanism differs from that of the phase separation driven by active compressive stress [18] or the tension difference, which is a well-known mechanism of conventional cell sorting. We examined the exerted tension on the boundary between motile-type cells and that between motile-type and nonmotile-type cells (see Appendix F) and found no significant tension difference in cell–cell boundary tension.

E. Pairwise translational and rotational cell motions drive antiparallel circulation

To understand how self-alignment leads to the antiparallel circulation pattern, we focused on interactions between motile-type cells. We simulated a simplified system consisting of a pair of motile-type cells ($N_\mathrm{c} = 20 \times 20, N_\mathrm{m} = 2$). We identified two stable modes of motion for the motile-type cell pair: translational motion and rotational motion [Figs. 6(a), 6(b) and Movie S4]. These modes emerge from the combined effects of the self-alignment and tension gradient. In the translational motion, the motile-type cells align in a head-to-tail configuration and migrate in the same direction while maintaining their contact [Fig. 6(a)]. In this process, the tension at the contact edge between the two cells nearly vanishes, as the opposing positive and negative tensions exerted by the rear and front cells cancel each other out, allowing the edge to maintain a finite length [Fig. 6(c)]. Once this configuration is established, the pair continues migrating as a single unit, unless disturbed by noise or shape fluctuations, owing to the persistence of polarity.

In the rotational motion, two motile-type cells persistently rotate as their polarities align in an antiparallel direction, resembling a yin-yang symbol [Fig. 6(b)]. This rotational motion can be explained by focusing on the torque acting on the edge shared by the motile-type cells. Specifically, when motile-type cells are positioned side-by-side with antiparallel polarity, each end of the shared edge connects to the rear edge of one of the cells (i). The tension gradient induces higher tension at these rear edges, generating a torque that drives the rotation of the shared edge. As a result of this tension, the length of the shared edge initially shrinks (ii). Before the edge length reaches zero, i.e., before the cells fully separate, the tension decreases and becomes negative, causing the edge to elongate again (iii–iv) (see Appendix G). This process is cyclically repeated, allowing the cells to rotate continuously. Consequently, the tension at the shared edge oscillates periodically around zero, and the edge length oscillates at the same frequency [Fig. 6(c)]. This rotation may also be sustained by confinement from surrounding nonmotile-type cells [65].

The cell configurations in the translational and rotational modes correspond to the preferred adjacent cell alignments observed in the pairwise order S [Fig. 4(c)]. Specifically, cells located front-to-back tend to align in the same direction, consistent with the translational mode, while cells located side-by-side tend to align in opposite directions, corresponding to the rotational mode. These findings suggest that unidirectional alignment of cells in rows, and their rotation within the domain, arise from the intrinsic two-cell behaviors in this system.

F. *D. discoideum* demonstrates an antiparallel circulation pattern

To explore the relevance of antiparallel circulation patterns in biological systems, we focused on the collective cell movements of *D. discoideum*. These cells are monopolar and motile, showing a vortex-like motion [37] even in the absence of chemotactic signals [83]. Notably, cell polarity is determined by front-to-back cell–cell contacts [83], which is consistent with the preferred configurations observed in our model [Fig. 4(c)]. This led us to anticipate that an antiparallel circulating state may have been overlooked due to the complexity of cell movement in three-dimensional (3D) space. To identify cell movements clearly, we simplified the system by confining the differentiated cells to two dimensions (see Appendix H). This was achieved by seeding the cells in a custom-made chamber of 2.5 μm thickness, placed between a glass coverslip and polydimethylsiloxane [84,85]. In the resulting disk-like aggregate [Fig. 7(a)], we found an antiparallel circulation pattern similar to that observed in our simulations [Fig. 7(b) and Movie S5].

To quantify this observation, we calculated the direction and speed statistics of cell movements [Fig. 7(c)]. The results showed that cells predominantly move in either a clockwise or counterclockwise direction, and their velocities are highest in the respective tangential directions,

indicating that the cells migrate in a concentric antiparallel manner. For most cells, the persistent time of the migration direction, denoted as τ_α (see Appendix H), was longer than 500 seconds. Cells with short persistent times were rare in the actual data compared with those in bootstrap resampled data [Fig. 7(d)]. This finding indicates that the observed cell circulation persists for a significant duration. These results demonstrate that *D. discoideum* cells exhibit continuous, concentric antiparallel circulation patterns similar to those predicted in our simulations. We should note that these circulations were not single rows, but instead a few cells wide, potentially due to the side-by-side cell adhesion [86], which differs from the patterns seen in the simulations.

Lastly, to investigate the elementary processes of antiparallel cell circulation in *D. discoideum*, we observed pairwise cell movements. By seeding cells at a lower concentration, we identified two characteristic cell motions in two-cell clusters. The first is a translational movement, where the cells align in a head-to-tail configuration [Fig. 7(e)]. This configuration persists until the pair encounters and collides with another cluster, often a larger cluster. This behavior closely resembles the migration patterns of 2D cell clusters under an imposed gradient of the chemoattractant cAMP [83]. The second is a rotational movement, frequently observed when cAMP synthesis is pharmacologically inhibited to eliminate long-range directional cues between separate clusters [Fig. 7(f)]. In this mode, the cells rotate either clockwise or counterclockwise while maintaining their configuration. These results suggest that *D. discoideum* exhibits the elementary processes required for group-level antiparallel cell circulation, i.e., translational and rotational motions between contacting cells, which closely agree with the cell behaviors driven by self-alignment combined with the tension gradient observed in our simulations [Figs. 6(a) and 6(b)]. These findings highlight the antiparallel circulating state as a generic emergent property of polar motile cells.

IV. DISCUSSION

Our results demonstrate that self-alignment combined with a tension gradient induces phase separation by forming stable domains of polar motile cells. Within each domain, cells self-organize into a dynamic structure characterized by concentric antiparallel circulations. To the best of our knowledge, such antiparallel circulations have not been reported in models based on MIPS, mutual alignment, or self-alignment. While both mutual alignment and self-alignment can produce vortices, the circulations within each vortex are typically unidirectional, which distinguishes our model from existing models.

The relationship between cell speed and the degree of cell ordering highlights a marked deviation from typical phase separation behaviors. As the separation degree μ increases over time t [Fig. 2(b)], the speed of motile-type cells also increases [Fig. 4(e)], in contrast to MIPS, where

particle speed decreases during phase separation [31]. This finding reflects a fundamental difference in the phase separation mechanism. In MIPS, particles aggregate because of speed reduction from repeated deposition. In contrast, in our model, cells aggregate through enhanced speed driven by the emergence of circulation ordering. The resulting continuous flow generates a normal stress difference [Fig. 5], which in turn drives phase separation. These findings suggest a positive feedback loop between macroscopic ordering and microscopic cell motions. Initially, the system is disordered due to frequent cell collisions; however, it gradually self-organizes into coherent circulation patterns that stabilize the ordered structure and enable cohesive collective migration. Each circulating loop acts as a guiding rail, supporting continuous cell migration and maintaining local alignment. This distinct mechanism highlights the central role of circulation in driving phase separation.

While our model is based on self-alignment, it departs from conventional self-alignment models. Existing self-alignment models do not exhibit phase separation accompanied by antiparallel circulations or vortex patterns. These models typically produce either flocking behavior [40,47,49] or vortex-like motion [87]. In a rare case where phase separation occurs, it is the nonmotile cells that aggregate [47]. In a model that generates vortex patterns, geometric constraints are required to sustain circulation, and phase separation is absent [87]. Furthermore, a pioneering study using the Potts model demonstrated vortex patterns driven by velocity-aligned self-propulsion [37], in which cell polarity is determined by the velocities of neighboring cells—a mechanism that is akin to mutual alignment rather than self-alignment.

Our model also differs from Vicsek-type and other mutual alignment-based models, not only in the emergent patterns but also in the underlying mechanisms of phase separation. For example, some Vicsek-type models produce spontaneously emerging vortices [44,45,88–90]; some exhibit singular, unidirectional circulation [46], and others generate stable, disk-like structures [45,91]. In these models, phase separation typically requires additional mechanisms, such as cell mobility that depends on local polarity orientation [91], or non-reciprocal interactions that introduce a preferred rotational angle to generate torque [45,92]. Moreover, domain growth in Vicsek models proceeds via large density fluctuations driven by polar ordering [93], leading to diffusion-independent dynamics reminiscent of gas–liquid phase separation [94]. In contrast, our model maintains density within compacted systems, and domain growth is constrained by diffusion [Fig. 3]. This contrast in domain behavior highlights the uniqueness of the observed phase separation.

The key cell behaviors that drive phase separation in our model are elementary cell motions, particularly the pairwise rotational mode [Fig. 6]. This motion can arise from self-alignment but, to the best of our knowledge, has not been reported to originate from mutual alignment [65]. While mutual alignment promotes local ordering of cell orientation, making antiparallel configurations

unfavored in principle, self-alignment does not uniquely determine the spatial order of adjacent cells. In our system, the interplay between self-alignment and a tension gradient favors both pairwise translational and rotational motions, leading to the emergence of antiparallel circulations.

These features highlight a unique phase separation mechanism, setting our model apart from those previously established. On the basis of this central thesis, we suggest referring to the phenomenon as "circulation-induced phase separation" (CirPS). Other models employing different force-generating mechanisms that effectively drive translational and rotational motions may exhibit CirPS—Likewise, because key cellular behaviors underlying CirPS—translational and rotational motions—are frequently observed [83,95–99], we expect CirPS to be involved in various multicellular dynamics. In the present study, we demonstrated the antiparallel co-existence of circulating states in 2D aggregates of *D. discoideum* [Fig. 7]. The appearance of reorienting cells is thought to be important for breaking up *D. discoideum* aggregates [100]; thus, the antiparallel phase separation may underlie its aggregate size regulation and may also play a role during cell type-dependent cell sorting. Similar mechanisms may also be at work in breaking up tumor clusters. Overall, CirPS represents a distinct phase separation mechanism in cell collectives that potentially underlies movements, arrangements, and ordering of polar cells.

ACKNOWLEDGEMENTS

We thank all the members of the Okuda Laboratory for their discussions. This work was supported by the WISE Program for Nano-Precision Medicine, Science, and Technology of Kanazawa University, Ministry of Education, Culture, Sports, Science and Technology (MEXT); the Japan Science and Technology Agency (JST), CREST [Grant No. JPMJCR1921, JPMJCR24B2, JPMJCR1923]; the Japan Society for the Promotion of Science (JSPS), KAKENHI [Grant No. 21K15081, 22H05170, 23H00384, 23H04304, 24H01398, 24H01937, 25K01118, 25H01363, 25H01771, 25K22468]; the Japanese Agency for Medical Research and Development (AMED), a Program for Technological Innovation of Regenerative Medicine Grant [23bm0704065h0003], and the World Premier International Research Center Initiative, MEXT, Japan.

DATA AVAILABILITY

The data that support the findings of this article are openly available [citation number to be inserted here].

References

[1] M. S. Steinberg, On the mechanism of tissue reconstruction by dissociated cells. I. Population kinetics, differential adhesiveness. and the absence of directed migration, Proc. Natl. Acad. Sci. U. S. A. **48**, 1577 (1962).

[2] J.-P. Rieu and Y. Sawada, Hydrodynamics and cell motion during the rounding of two dimensional hydra cell aggregates, Eur. Phys. J. B **27**, 167 (2002).

[3] S. F. G. Krens and C.-P. Heisenberg, Cell sorting in development, Curr. Top. Dev. Biol. **95**, 189 (2011).

[4] S. Asakura and F. Oosawa, Interaction between particles suspended in solutions of macromolecules, J. Polym. Sci. **33**, 183 (1958).

[5] T. Biben, P. Bladon, and D. Frenkel, Depletion effects in binary hard-sphere fluids, J. Phys. Condens. Matter **8**, 10799 (1996).

[6] B. Götzelmann, R. Evans, and S. Dietrich, Depletion forces in fluids, Phys. Rev. E Stat. Phys. Plasmas Fluids Relat. Interdiscip. Topics **57**, 6785 (1998).

[7] M. Dijkstra and D. Frenkel, Evidence for entropy-driven demixing in hard-core fluids, Phys. Rev. Lett. **72**, 298 (1994).

[8] Y. Mao, M. E. Cates, and H. N. W. Lekkerkerker, Depletion force in colloidal systems, Physica A **222**, 10 (1995).

[9] N. Rivas, S. Ponce, B. Gallet, D. Risso, R. Soto, P. Cordero, and N. Mujica, Sudden chain energy transfer events in vibrated granular media, Phys. Rev. Lett. **106**, 088001 (2011).

[10] N. Rivas, P. Cordero, D. Risso, and R. Soto, Segregation in quasi-two-dimensional granular systems, New J. Phys. **13**, 055018 (2011).

[11] E. F. Teixeira, C. P. Beatrici, H. C. M. Fernandes, and L. G. Brunnet, Segregation in Binary Mixture with Differential Contraction among Active Rings, Phys. Rev. Lett. **134**, (2025).

[12] S. R. McCandlish, A. Baskaran, and M. F. Hagan, Spontaneous segregation of self-propelled particles with different motilities, Soft Matter **8**, 2527 (2012).

[13] J. Stenhammar, R. Wittkowski, D. Marenduzzo, and M. E. Cates, Activity-induced phase separation and self-assembly in mixtures of active and passive particles, Phys. Rev. Lett. **114**, 018301 (2015).

[14] S. N. Weber, C. A. Weber, and E. Frey, Binary mixtures of particles with different diffusivities demix, Phys. Rev. Lett. **116**, 058301 (2016).

[15] R.-X. Guo, J.-J. Li, and B.-Q. Ai, Chirality-induced phase separation and collective dynamics in binary mixtures of chiral particles, Phys. Rev. E. **111**, 045423 (2025).

[16] L. Balasubramaniam et al., Investigating the nature of active forces in tissues reveals how contractile cells can form extensile monolayers, Nat. Mater. **20**, 1156 (2021).

[17] S. Bhattacharyya and J. M. Yeomans, Phase separation driven by active flows, Phys. Rev. Lett.

130, 238201 (2023).
[18] J. Rozman and J. M. Yeomans, Cell sorting in an active nematic vertex model, Phys. Rev. Lett. **133**, 248401 (2024).
[19] F. Graner and J. A. Glazier, Simulation of biological cell sorting using a two-dimensional extended Potts model, Phys. Rev. Lett. **69**, 2013 (1992).
[20] J. A. Glazier and F. Graner, Simulation of the differential adhesion driven rearrangement of biological cells, Phys. Rev. E Stat. Phys. Plasmas Fluids Relat. Interdiscip. Topics **47**, 2128 (1993).
[21] J. C. Mombach, J. A. Glazier, R. C. Raphael, and M. Zajac, Quantitative comparison between differential adhesion models and cell sorting in the presence and absence of fluctuations, Phys. Rev. Lett. **75**, 2244 (1995).
[22] R. A. Foty and M. S. Steinberg, The differential adhesion hypothesis: a direct evaluation, Dev. Biol. **278**, 255 (2005).
[23] M. Durand, Large-scale simulations of biological cell sorting driven by differential adhesion follow diffusion-limited domain coalescence regime, PLoS Comput. Biol. **17**, e1008576 (2021).
[24] A. Nakajima and S. Ishihara, Kinetics of the cellular Potts model revisited, New J. Phys. **13**, 033035 (2011).
[25] E. Batlle and D. G. Wilkinson, Molecular mechanisms of cell segregation and boundary formation in development and tumorigenesis, Cold Spring Harb. Perspect. Biol. **4**, a008227 (2012).
[26] J. D. Amack and M. L. Manning, Knowing the boundaries: extending the differential adhesion hypothesis in embryonic cell sorting, Science **338**, 212 (2012).
[27] S. Pawlizak et al., Testing the differential adhesion hypothesis across the epithelial−mesenchymal transition, New Journal of Physics **17**, (2015).
[28] J. Tailleur and M. E. Cates, Statistical mechanics of interacting run-and-tumble bacteria, Phys. Rev. Lett. **100**, 218103 (2008).
[29] Y. Fily and M. C. Marchetti, Athermal phase separation of self-propelled particles with no alignment, Phys. Rev. Lett. **108**, 235702 (2012).
[30] I. Buttinoni, J. Bialké, F. Kümmel, H. Löwen, C. Bechinger, and T. Speck, Dynamical clustering and phase separation in suspensions of self-propelled colloidal particles, Phys. Rev. Lett. **110**, 238301 (2013).
[31] M. E. Cates and J. Tailleur, Motility-Induced Phase Separation, Annual Review of Condensed Matter Physics **6**, 219 (2015).
[32] G. Liu, A. Patch, F. Bahar, D. Yllanes, R. D. Welch, M. C. Marchetti, S. Thutupalli, and J. W. Shaevitz, Self-driven phase transitions drive Myxococcus xanthus fruiting body formation, Phys. Rev. Lett. **122**, 248102 (2019).
[33] J. M. Belmonte, G. L. Thomas, L. G. Brunnet, R. M. C. de Almeida, and H. Chaté, Self-propelled particle model for cell-sorting phenomena, Phys. Rev. Lett. **100**, 248702 (2008).

[34] C. P. Beatrici and L. G. Brunnet, Cell sorting based on motility differences, Phys. Rev. E Stat. Nonlin. Soft Matter Phys. **84**, 031927 (2011).

[35] C. Strandkvist, J. Juul, B. Baum, A. J. Kabla, and T. Duke, A kinetic mechanism for cell sorting based on local variations in cell motility, Interface Focus **4**, 20140013 (2014).

[36] D. Sarkar, G. Gompper, and J. Elgeti, A minimal model for structure, dynamics, and tension of monolayered cell colonies, Commun. Phys. **4**, (2021).

[37] W.-J. Rappel, A. Nicol, A. Sarkissian, H. Levine, and W. F. Loomis, Self-organized vortex state in two-DimensionalDictyosteliumDynamics, Phys. Rev. Lett. **83**, 1247 (1999).

[38] B. Szabó, G. J. Szöllösi, B. Gönci, Z. Jurányi, D. Selmeczi, and T. Vicsek, Phase transition in the collective migration of tissue cells: experiment and model, Phys. Rev. E Stat. Nonlin. Soft Matter Phys. **74**, 061908 (2006).

[39] P. Y. Hwang, A. Brenot, A. C. King, G. D. Longmore, and S. C. George, Randomly distributed K14+ breast tumor cells polarize to the leading edge and guide collective migration in response to chemical and mechanical environmental cues, Cancer Res. **79**, 1899 (2019).

[40] K. Matsushita, T. Arakaki, and K. Fujimoto, Motion ordering in cellular polar–polar and polar–nonpolar interactions, J. Phys. Soc. Jpn. **93**, (2024).

[41] Q. J. Braat, C. Storm, and L. Janssen, Formation of motile cell clusters in heterogeneous model tumors: the role of cell-cell alignment, Phys. Rev. E **110**, 064401 (2024).

[42] S. Okuda and K. Sato, Polarized interfacial tension induces collective migration of cells, as a cluster, in a 3D tissue, Biophys. J. **121**, 1856 (2022).

[43] A. Martín-Gómez, D. Levis, A. Díaz-Guilera, and I. Pagonabarraga, Collective motion of active Brownian particles with polar alignment, Soft Matter **14**, 2610 (2018).

[44] A. Costanzo and C. K. Hemelrijk, Spontaneous emergence of milling (vortex state) in a Vicsek-like model, J. Phys. D Appl. Phys. **51**, 134004 (2018).

[45] T. Hiraiwa, Dynamic self-organization of idealized migrating cells by contact communication, Phys. Rev. Lett. **125**, 268104 (2020).

[46] Y. Wu, J. Li, D. Chen, X. Li, and H.-T. Zhang, Pattern phase transitions in 3D minimal Vicsek model, EPL **134**, 50004 (2021).

[47] A. J. Kabla, Collective cell migration: leadership, invasion and segregation, J. R. Soc. Interface **9**, 3268 (2012).

[48] C. Malinverno et al., Endocytic reawakening of motility in jammed epithelia, Nat. Mater. **16**, 587 (2017).

[49] F. Giavazzi Università degli Studi di Milano, Dipartimento di Biotecnologie Mediche e Medicina Traslazionale, 20090 Segrate, Italy. roberto. cerbino@unimi. it, M. Paoluzzi, M. Macchi, D. Bi, G. Scita, M. L. Manning, R. Cerbino, and M. C. Marchetti, Flocking transitions in confluent tissues, Soft Matter **14**, 3471 (2018).

[50] V. Petrolli et al., Confinement-induced transition between wavelike collective cell migration modes, Phys. Rev. Lett. **122**, 168101 (2019).

[51] Y. Shen, J. O'Byrne, A. Schoenit, A. Maitra, R.-M. Mège, R. Voituriez, and B. Ladoux, Flocking and giant fluctuations in epithelial active solids, Proc. Natl. Acad. Sci. U. S. A. **122**, e2421327122 (2025).

[52] M. Bergert, A. Erzberger, R. A. Desai, I. M. Aspalter, A. C. Oates, G. Charras, G. Salbreux, and E. K. Paluch, Force transmission during adhesion-independent migration, Nat. Cell Biol. **17**, 524 (2015).

[53] K. Sato, T. Hiraiwa, and T. Shibata, Cell chirality induces collective cell migration in epithelial sheets, Phys. Rev. Lett. **115**, 188102 (2015).

[54] K. Sato, T. Hiraiwa, E. Maekawa, A. Isomura, T. Shibata, and E. Kuranaga, Left-right asymmetric cell intercalation drives directional collective cell movement in epithelial morphogenesis, Nat. Commun. **6**, 10074 (2015).

[55] A. Shellard, A. Szabó, X. Trepat, and R. Mayor, Supracellular contraction at the rear of neural crest cell groups drives collective chemotaxis, Science **362**, 339 (2018).

[56] S. Okuda, E. Kuranaga, and K. Sato, Apical Junctional Fluctuations Lead to Cell Flow while Maintaining Epithelial Integrity, Biophys. J. **116**, 1159 (2019).

[57] K. Sato, A cell membrane model that reproduces cortical flow-driven cell migration and collective movement, Front. Cell Dev. Biol. **11**, 1126819 (2023).

[58] H. Honda and G. Eguchi, How much does the cell boundary contract in a monolayered cell sheet?, J. Theor. Biol. **84**, 575 (1980).

[59] R. Farhadifar, J.-C. Röper, B. Aigouy, S. Eaton, and F. Jülicher, The influence of cell mechanics, cell-cell interactions, and proliferation on epithelial packing, Curr. Biol. **17**, 2095 (2007).

[60] A. G. Fletcher, M. Osterfield, R. E. Baker, and S. Y. Shvartsman, Vertex models of epithelial morphogenesis, Biophys. J. **106**, 2291 (2014).

[61] S. Alt, P. Ganguly, and G. Salbreux, Vertex models: from cell mechanics to tissue morphogenesis, Philos. Trans. R. Soc. Lond. B Biol. Sci. **372**, (2017).

[62] G. Erdemci-Tandogan and M. L. Manning, Effect of cellular rearrangement time delays on the rheology of vertex models for confluent tissues, PLoS Comput. Biol. **17**, e1009049 (2021).

[63] S. Henkes, Y. Fily, and M. C. Marchetti, Active jamming: self-propelled soft particles at high density, Phys. Rev. E Stat. Nonlin. Soft Matter Phys. **84**, 040301 (2011).

[64] M. Basan, J. Elgeti, E. Hannezo, W.-J. Rappel, and H. Levine, Alignment of cellular motility forces with tissue flow as a mechanism for efficient wound healing, Proc. Natl. Acad. Sci. U. S. A. **110**, 2452 (2013).

[65] B. A. Camley, Y. Zhang, Y. Zhao, B. Li, E. Ben-Jacob, H. Levine, and W.-J. Rappel, Polarity mechanisms such as contact inhibition of locomotion regulate persistent rotational motion of mammalian cells on micropatterns, Proc. Natl. Acad. Sci. U. S. A. **111**, 14770 (2014).

[66] B. A. Camley and W.-J. Rappel, Velocity alignment leads to high persistence in confined cells, Phys. Rev. E Stat. Nonlin. Soft Matter Phys. **89**, 062705 (2014).

[67] K.-D. N. T. Lam, M. Schindler, and O. Dauchot, Self-propelled hard disks: implicit alignment

and transition to collective motion, New J. Phys. **17**, 113056 (2015).
[68] P. Baconnier, O. Dauchot, V. Démery, G. Düring, S. Henkes, C. Huepe, and A. Shee, Self-aligning polar active matter, Rev. Mod. Phys. **97**, (2025).
[69] D. Bi, X. Yang, M. C. Marchetti, and M. L. Manning, Motility-driven glass and jamming transitions in biological tissues, Phys. Rev. X. **6**, (2016).
[70] A. J. Bray, Theory of phase-ordering kinetics, Adv. Phys. **51**, 481 (2002).
[71] A. G. Thompson, J. Tailleur, M. E. Cates, and R. A. Blythe, Lattice models of nonequilibrium bacterial dynamics, J. Stat. Mech. **2011**, P02029 (2011).
[72] G. S. Redner, M. F. Hagan, and A. Baskaran, Structure and dynamics of a phase-separating active colloidal fluid, Phys. Rev. Lett. **110**, 055701 (2013).
[73] J. Stenhammar, D. Marenduzzo, R. J. Allen, and M. E. Cates, Phase behaviour of active Brownian particles: the role of dimensionality, Soft Matter **10**, 1489 (2014).
[74] S. Dey, D. Das, and R. Rajesh, Spatial structures and giant number fluctuations in models of active matter, Phys. Rev. Lett. **108**, 238001 (2012).
[75] N. Katyal, S. Dey, D. Das, and S. Puri, Coarsening dynamics in the Vicsek model of active matter, Eur. Phys. J. E Soft Matter **43**, 10 (2020).
[76] H. Furukawa, Kinetics of droplet growth in systems with arbitrary degeneracy, Phys. Rev. A **29**, 2160 (1984).
[77] M. Kolb, Unified Description of Static and Dynamic Scaling for Kinetic Cluster Formation, Phys. Rev. Lett. **53**, 1653 (1984).
[78] P. Meakin, Diffusion-limited droplet coalescence, Physica A **165**, 1 (1990).
[79] C. P. Beatrici, R. M. C. de Almeida, and L. G. Brunnet, Mean-cluster approach indicates cell sorting time scales are determined by collective dynamics, Phys. Rev. E. **95**, 032402 (2017).
[80] I. M. Lifshitz and V. V. Slyozov, The kinetics of precipitation from supersaturated solid solutions, J. Phys. Chem. Solids **19**, 35 (1961).
[81] T. M. Rogers and R. C. Desai, Numerical study of late-stage coarsening for off-critical quenches in the Cahn-Hilliard equation of phase separation, Phys. Rev. B Condens. Matter **39**, 11956 (1989).
[82] K. Weissenberg, A continuum theory of rheological phenomena, Nature **159**, 310 (1947).
[83] T. Fujimori, A. Nakajima, N. Shimada, and S. Sawai, Tissue self-organization based on collective cell migration by contact activation of locomotion and chemotaxis, Proc. Natl. Acad. Sci. U. S. A. **116**, 4291 (2019).
[84] T. Fujimori, H. Hashimura, and S. Sawai, Imaging-based analysis of cell-cell contact-dependent migration in Dictyostelium, Methods Mol. Biol. **2828**, 23 (2024).
[85] H. Hashimura, S. Kuwana, H. Nakagawa, K. Abe, T. Adachi, T. Sugita, S. Fujishiro, G. Honda, and S. Sawai, Multi-color fluorescence live-cell imaging in Dictyostelium discoideum, Cell Struct. Funct. **49**, 135 (2024).
[86] K. Müller and G. Gerisch, A specific glycoprotein as the target site of adhesion blocking Fab in

aggregating Dictyostelium cells, Nature **274**, 445 (1978).
[87] D. Canavello, R. H. Damascena, L. R. E. Cabral, and C. C. de Souza Silva, Polar order, shear banding, and clustering in confined active matter, Soft Matter **20**, 2310 (2024).
[88] S. Kayal, Department of Physics, Presidency University 86/1 College street, Kolkata-700073, India, M. Acharyya, and Department of Physics, Presidency University 86/1 College street, Kolkata-700073, India, Transient phases in the Vicsek model of flocking, J. Phys. Through Comput. **1**, 17 (2018).
[89] X. Wang, P.-C. Chen, K. Kroy, V. Holubec, and F. Cichos, Spontaneous vortex formation by microswimmers with retarded attractions, Nat. Commun. **14**, 56 (2023).
[90] D. Nishiguchi, S. Shiratani, K. A. Takeuchi, and I. S. Aranson, Vortex reversal is a precursor of confined bacterial turbulence, Proc. Natl. Acad. Sci. U. S. A. **122**, e2414446122 (2025).
[91] H. Xu and Y. Wu, Self-enhanced mobility enables vortex pattern formation in living matter, Nature **627**, 553 (2024).
[92] M. Fruchart, R. Hanai, P. B. Littlewood, and V. Vitelli, Non-reciprocal phase transitions, Nature **592**, 363 (2021).
[93] H. Chaté, Dry aligning dilute active matter, Annu. Rev. Condens. Matter Phys. **11**, 189 (2020).
[94] A. P. Solon, H. Chaté, and J. Tailleur, From phase to microphase separation in flocking models: the essential role of nonequilibrium fluctuations, Phys. Rev. Lett. **114**, 068101 (2015).
[95] C. Brangwynne, S. Huang, K. K. Parker, D. E. Ingber, and E. Ostuni, Symmetry breaking in cultured mammalian cells, In Vitro Cell. Dev. Biol. Anim. **36**, 563 (2000).
[96] A. Erzberger, A. Jacobo, A. Dasgupta, and A. J. Hudspeth, Mechanochemical symmetry breaking during morphogenesis of lateral-line sensory organs, Nat. Phys. **16**, 949 (2020).
[97] H. G. Lee and K. J. Lee, Neighbor-enhanced diffusivity in dense, cohesive cell populations, PLoS Comput. Biol. **17**, e1009447 (2021).
[98] E. L. Kozak, J. R. Miranda-Rodríguez, A. Borges, K. Dierkes, A. Mineo, F. Pinto-Teixeira, O. Viader-Llargués, J. Solon, O. Chara, and H. López-Schier, Quantitative videomicroscopy reveals latent control of cell-pair rotations in vivo, Development **150**, (2023).
[99] L. Lu et al., Polarity-driven three-dimensional spontaneous rotation of a cell doublet, Nat. Phys. **20**, 1194 (2024).
[100] J. Dallon, W. Jang, and R. H. Gomer, Mathematically modelling the effects of counting factor in Dictyostelium discoideum, Math. Med. Biol. **23**, 45 (2006).
[101] D. Bi, J. H. Lopez, J. M. Schwarz, and M. L. Manning, A density-independent rigidity transition in biological tissues, Nat. Phys. **11**, 1074 (2015).
[102] B. Loewe, M. Chiang, D. Marenduzzo, and M. C. Marchetti, Solid-liquid transition of deformable and overlapping active particles, Phys. Rev. Lett. **125**, 038003 (2020).
[103] M. Chiang, A. Hopkins, B. Loewe, D. Marenduzzo, and M. C. Marchetti, Multiphase field model of cells on a substrate: From three dimensional to two dimensional, Phys. Rev. E. **110**, 044403 (2024).

[104] D. A. Huse, Corrections to late-stage behavior in spinodal decomposition: Lifshitz-Slyozov scaling and Monte Carlo simulations, Phys. Rev. B Condens. Matter **34**, 7845 (1986).

[105] S. Ishihara and K. Sugimura, Bayesian inference of force dynamics during morphogenesis, J. Theor. Biol. **313**, 201 (2012).

[106] K. K. Chiou, L. Hufnagel, and B. I. Shraiman, Mechanical stress inference for two dimensional cell arrays, PLoS Comput. Biol. **8**, e1002512 (2012).

[107] X. Yang, D. Bi, M. Czajkowski, M. Merkel, M. L. Manning, and M. C. Marchetti, Correlating cell shape and cellular stress in motile confluent tissues, Proc. Natl. Acad. Sci. U. S. A. **114**, 12663 (2017).

[108] M. Skamrahl et al., Cellular segregation in cocultures is driven by differential adhesion and contractility on distinct timescales, Proc. Natl. Acad. Sci. U. S. A. **120**, e2213186120 (2023).

Appendices

APPENDIX A: EFFECTS OF TISSUE FLUIDITY ON PHASE SEPARATION

Varying cell properties such as deformability, motility, and noise can induce a jamming transition, during which tissue fluidity changes drastically [69,101–103]. To investigate the effects of tissue fluidity on phase separation, we first reproduced the jamming transition using our model. Here, we consider a tissue composed entirely of motile-type cells without self-alignment. In this model, the shape index p_0, the strength of the tension gradient γ^{p}, and the noise intensity D_r can be used to tune tissue fluidity, which corresponds to cell deformability, motility, and noise. For simplicity, the noise intensity was fixed at $D_r = 1$, and the mixing ratio and alignment rate were set to $\phi = 1$ and $J = 0$, respectively. To quantitatively assess tissue fluidity, we calculated the effective diffusion coefficient $D_{\mathrm{eff}} \coloneqq D_{\mathrm{s}}/D_0$, where D_{s} is the self-diffusion coefficient defined as $D_{\mathrm{s}} \coloneqq \mathrm{MSD}(\tau)/(4\tau)$ averaged for $\tau > 0.45T$, and D_0 is the free diffusion coefficient given by $D_0 \coloneqq 2\pi^2(\gamma^{\mathrm{p}}/\eta)^2/D_r$ [42,69] (see the Supplemental material for the detailed calculation of D_0). Here, $\mathrm{MSD}(\tau)$ denotes the mean-square displacement of motile-type cells at a time shift of τ (see Appendix C). We classified systems with $D_{\mathrm{eff}} < 10^{-3}$ as being a solid-like state and those with $D_{\mathrm{eff}} \geq 10^{-3}$ as fluid-like. As a result, we found that tissue fluidity transitions between solid-like and fluid-like states depended on the values of p_0 and γ^{p}, indicating that a jamming transition occurs [Fig. 8(a)].

We next considered a mixture of motile-type cells with self-alignment and nonmotile-type cells. In this case, the mixing ratio and noise intensity were set to $\phi = 0.5$ and $D_r = 1$. By varying p_0 and J, we observed that phase separation occurs only when the tissue is in a fluid-like state [Fig. 8(b)]. Based on these findings, all numerical simulations presented in the main text were performed under fluid-like conditions, as phase separation does not occur in the solid-like state.

APPENDIX B: DEPENDENCE ON THE INITIAL CONDITIONS

To investigate the dependence of phase separation on the initial conditions, we conducted simulations using both homogeneous and pre-separated initial states. The separated state was prepared by placing a circular domain of motile-type cells at the center of the system. When $J > D_r$, phase separation occurred regardless of the initial condition, although the degree of separation μ varied depending on the initial state [Fig. 9(a)]. In contrast, when $J < D_r$, the system eventually relaxed into a homogeneous state, irrespective of the initial condition, and μ converged to zero [Fig. 9(b)]. These results indicate that the occurrence of phase separation is not influenced by the initial condition. However, when phase separation does occur, the degree of separation is influenced by the

initial condition.

APPENDIX C: MACROSCOPIC BEHAVIOR OF THE CELLS AND DOMAINS

We calculated the MSD of motile-type cells during the time interval $T/2 \leq t \leq T$ as follows

$$\mathrm{MSD}(\tau) \coloneqq \frac{1}{(T/2)-\tau}\int_{T/2}^{T-\tau} \mathrm{d}t \left[\frac{1}{N_\mathrm{m}}\sum_{\alpha\in\mathcal{M}} \|\boldsymbol{r}_\alpha(\tau+t)-\boldsymbol{r}_\alpha(t)\|^2\right], \tag{8}$$

where τ is a time shift within the range $\tau \in [0, T/2)$. For short timescales, the ballistic diffusion regime ($\mathrm{MSD} \propto \tau^2$) expanded as the system transitioned from a homogeneous to a phase separation state by varying the alignment rate [Fig. 3(a)]. This expansion is attributed to the increased persistence of motile-type cells when $J/D_r > 1$ [66].

For longer timescales, we observed subdiffusive behavior characterized by $\mathrm{MSD} \propto \tau^\lambda$ with $\lambda < 1$ when J was sufficiently large, indicating restricted motion of motile-type cells under complete phase separation. In contrast, when J was small, we found normal diffusion behavior characterized by $\mathrm{MSD} \propto \tau^1$, where motion was primarily governed by noise.

Next, we examined the time evolution of the typical domain size. To simplify the calculation, we first define the "existence probability" $f_\alpha(\boldsymbol{x}, t)$ of the α-th cell at coordinate $\boldsymbol{x}$ as

$$f_\alpha(\boldsymbol{x}, t) \coloneqq \frac{1}{\sqrt{2\pi}\sigma}\exp\left[-\frac{\|\boldsymbol{x}-\boldsymbol{r}_\alpha(t)\|^2}{2\sigma^2}\right], \tag{9}$$

where σ is the standard deviation of f_α, regarded as a spatial scale of a single cell. We set $\sigma = 1/2\sqrt{\pi}$ for all cells, which is equal to half of the radius of the circle with unit area. Using f_α, we introduced the distribution function of motile-type cells, $f(\boldsymbol{x}, t)$, defined as

$$f(\boldsymbol{x}, t) \coloneqq \frac{1}{N_\mathrm{c}}\sum_{\alpha=1}^{N_\mathrm{c}} \omega_\alpha f_\alpha(\boldsymbol{x}, t), \tag{10}$$

where ω_α is given by

$$\omega_\alpha = \begin{cases} 1 & (\alpha \in \mathcal{M}) \\ -1 & (\alpha \in \mathcal{N}) \end{cases}. \tag{11}$$

Note that f can be negative when nonmotile-type cells are near coordinate $\boldsymbol{x}$. Using f, we defined the spatial correlation function of cell types $C(r, t)$ [23,24,104] as

$$C(r, t) \coloneqq \langle s(\boldsymbol{x}_0, t)s(\boldsymbol{x}_0+\boldsymbol{x}, t)\rangle - \langle s(\boldsymbol{x}_0, t)\rangle^2, \tag{12}$$

where $r = \|\boldsymbol{x}\|$ and $s(\boldsymbol{x}, t) = \mathrm{sgn}\, f(\boldsymbol{x}, t)$. The average $\langle\cdot\rangle$ is taken over the coordinate $\boldsymbol{x}_0$ and

the displacement $\boldsymbol{x}$ with the given distance of $r = \|\boldsymbol{x}\|$. The domain size $R(t)$ is defined as the first zero-crossing point of the correlation function $C(r,t)$, i.e.,

$$R(t) \coloneqq \min\{\, r \mid C(r,t) \leq 0\}. \tag{13}$$

We first confirmed that $C(r,t)$ for different time points converged to the same curve as a function of $r/R(t)$ [Fig. 3(d)]. Furthermore, domain size follows $R \propto t^{\nu}$ with growth exponent ν, which indicates the mechanisms of domain growth. Under conditions in which the noise intensity is very low ($D_r \lesssim 0.25$) and the alignment rate is moderate ($J \lesssim 7$), $\nu \approx 1/3$ [Figs. 3(b), 3(c) and 10(a)], suggesting that the domain growth is governed by diffusion [81]. As the noise intensity or the alignment rate increases ($J \gtrsim 7$), the growth exponent rapidly shifts to $\nu \approx 1/4$ [Figs. 3(b), 3(c) and 10(a), 10(b)], suggesting that the domain growth is dominated by direct domain coalescence (diffusion-coalescence) processes [76–79].

APPENDIX D: CALCULATION OF THE CIRCULATION VELOCITY

To quantify the antiparallel circulation pattern, we calculated the speed and direction of motile cell motion with respect to the center of circulation $\widetilde{\boldsymbol{R}}(t)$ for each domain, which was determined from the velocity profile at each time t as follows. Using the velocity vector $\boldsymbol{v}_\alpha$ and the position vector $\boldsymbol{r}_\alpha - \widetilde{\boldsymbol{R}}$, which connects the circulation center and the centroid of the α-th cell, $\widetilde{\boldsymbol{R}}(t)$ is defined as the point $\boldsymbol{R}'$ that minimizes the following function

$$\sum_{\alpha=1}^{N_\mathrm{c}} [\boldsymbol{v}_\alpha \cdot (\boldsymbol{r}_\alpha - \boldsymbol{R}')]^2. \tag{14}$$

The optimal circulation center $\widetilde{\boldsymbol{R}}$ can be written explicitly as

$$\widetilde{\boldsymbol{R}} = \left(\sum_{\alpha=1}^{N_\mathrm{c}} \boldsymbol{v}_\alpha \boldsymbol{v}_\alpha^\top \right)^{-1} \left(\sum_{\alpha=1}^{N_\mathrm{c}} \boldsymbol{v}_\alpha \boldsymbol{v}_\alpha^\top \boldsymbol{r}_\alpha \right). \tag{15}$$

Next, the circulation velocity v_α^{circ} of the α-th cell at each time point was calculated as the projection of its velocity vector onto the tangential direction of the circular path. This is defined as

$$v_\alpha^{\mathrm{circ}} \coloneqq \frac{\boldsymbol{v}_\alpha \wedge (\boldsymbol{r}_\alpha - \widetilde{\boldsymbol{R}})}{\|\boldsymbol{r}_\alpha - \widetilde{\boldsymbol{R}}\|} = \frac{v_{\alpha x}(r_{\alpha y} - \tilde{R}_y) - v_{\alpha y}(r_{\alpha x} - \tilde{R}_x)}{\sqrt{(r_{\alpha x} - \tilde{R}_x)^2 + (r_{\alpha y} - \tilde{R}_y)^2}}. \tag{16}$$

Here, v_α^{circ} is positive when the cell is circulating in the clockwise direction. Figures 3(a) and 7(a) show the spatial pattern of the circulation direction, as indicated by the sign of v_α^{circ} at a single time point. These findings clearly exhibit an antiparallel circulation pattern.

APPENDIX E: CALCULATION OF THE STRESS TENSOR

To obtain the stress tensor for each cell, we first define the energy function U_α of the α-th cell as follows

$$U_\alpha = \frac{K_\mathrm{A}}{2}(A_\alpha - A_0)^2 + \frac{K_\mathrm{P}}{2}(P_\alpha - P_0)^2 + \sum_{\varepsilon \in \mathcal{E}_\alpha} \gamma_{\alpha\varepsilon} l_\varepsilon. \tag{17}$$

The total energy as determined by Eq. (2) can be divided into each cell as $U = \sum_{\alpha=1}^{N_\mathrm{c}} U_\alpha$. Based on U_α, the stress tensor σ_{ij}^α of the α-th cell is defined as

$$\sigma_{ij}^\alpha \coloneqq \frac{\partial U_\alpha}{\partial A_\alpha}\delta_{ij} + \frac{1}{A_\alpha}\sum_{\varepsilon \in \mathcal{E}_\alpha} \frac{\partial U_\alpha}{\partial r_i^\varepsilon} r_j^\varepsilon, \tag{18}$$

where i and j denote Cartesian coordinates, δ_{ij} is the Kronecker delta, and r_i^ε represents the i-th component of the edge vector joining the vertices that make up the ε-th edge [105–107]. From Eqs. (13) and (14), the explicit form of the stress tensor becomes

$$\sigma_{ij}^\alpha = K_\mathrm{A}(A_\alpha - A_0)\delta_{ij} + \frac{1}{A_\alpha}\sum_{\varepsilon \in \mathcal{E}_\alpha} [K_\mathrm{P}(P_\alpha - P_0) + \gamma_{\alpha\varepsilon}] \frac{r_i^\varepsilon}{l_\varepsilon} r_j^\varepsilon. \tag{19}$$

The two eigenvalues of the stress tensor, σ_1^α and σ_2^α ($\sigma_1^\alpha > \sigma_2^\alpha$), correspond to the maximum and minimum principal stresses, respectively. The eigenvectors $\boldsymbol{d}_k^\alpha$ (with $k = 1,2$) associated with these eigenvalues indicate the directions of the principal stresses. To examine the anisotropy of stress with respect to hydrostatic pressure, we defined the deviatoric stress $\tilde{\sigma}_k^\alpha$ as

$$\tilde{\sigma}_k^\alpha \coloneqq \sigma_k^\alpha + p^\alpha, \tag{20}$$

where $p^\alpha \coloneqq -(\sigma_1^\alpha + \sigma_2^\alpha)/2$ is the hydrostatic pressure of the α-th cell. By this definition, we obtain $\tilde{\sigma}_1^\alpha \geq 0$ and $\tilde{\sigma}_2^\alpha \leq 0$. This means that tensile stress acts along the direction of the maximum principal stress, while compressive stress acts along the direction of the minimum principal stress. If normal stress differences emerge, deviatoric stresses satisfy $\tilde{\sigma}_k^\alpha \neq 0$. We refer to the direction $\boldsymbol{d}_1^\alpha$ as the tensile principal stress direction and $\boldsymbol{d}_2^\alpha$ as the compressive principal stress direction.

Next, we calculated the angle δ_α, which measures the alignment between the tensile principal stress direction and the radial direction from the center of circulation to the cell centroid. This angle is defined as

$$\delta_\alpha = \arccos\left[\frac{(\boldsymbol{r}_\alpha - \tilde{\boldsymbol{R}}) \cdot \boldsymbol{d}_1^\alpha}{\|\boldsymbol{r}_\alpha - \tilde{\boldsymbol{R}}\|}\right]. \tag{21}$$

Assuming the domain is circular, values of δ_α closer to $\pi/2$ indicate that the stress director is more aligned with the circumferential direction of the domain.

APPENDIX F: TENSION DIFFERENCE

Many studies have shown that cell sorting can be driven by differences in interfacial tension between like and unlike cell types and that the system reaches a sorted state as a final equilibrium state [1,19,22,108]. However, our system is maintained in a non-equilibrium state due to the presence of a tension gradient in motile-type cells, and the model does not explicitly incorporate any inherent tension differences. To investigate whether an effective tension difference might drive phase separation in our system, we calculated and compared the interfacial tension between motile-type and nonmotile-type cells. The results showed no significant difference in tension between these boundaries, even in cases where phase separation occurred [Fig. 11]. This finding indicates that the phase separation observed in our system is not driven by tension differences, distinguishing it from conventional cell sorting mechanisms.

APPENDIX G: STABILITY OF THE ROTATIONAL MODE

In the rotational mode of motile-type cell pairs, the tension and length of the interfacial edge of the cell pair oscillate with the same frequency and the edge does not vanish, resulting in the rotational motion and cell adhesion being preserved. To verify this, we compared the simulation results with results from an idealized system. The time variation of edge length l with a harmonic oscillating tension $\gamma(t) = A_\gamma \cos \omega t$ with amplitude A_γ in an overdamped system with friction coefficient η is given by $\mathrm{d}l/\mathrm{d}t = \gamma/\eta$. Integrating this equation, we can obtain $l(t) = l_0 + \left(A_\gamma/\eta\omega\right) \sin \omega t$, where l_0 is the equilibrium length of the edge. Based on the definition of the time unit and results shown in Fig. 6(c) in terms of $0 \leq t \leq 50$, we estimated $\eta = 1.0$, $l_0 \approx 1.0$, $A_\gamma \approx 1.5\gamma^{\mathrm{p}} = 0.30$, and $\omega = 2\pi/T_{\mathrm{o}} \approx 1.0$, where T_{o} is the oscillation period. Substituting these values into the equation of $l(t)$ yields the maximum and minimum values of the edge length: $l_{\mathrm{max}} = l_0 + A_\gamma/\eta\omega \approx 1.3$ and $l_{\mathrm{min}} = l_0 - A_\gamma/\eta\omega \approx 0.7$, which are roughly consistent with the results in Fig. 6(c). Moreover, as satisfying $l_{\mathrm{min}} \approx 0.7 > 0$, the interfacial edge does not vanish even if the tension oscillates with the given values of η, l_0, ω, and A_γ.

APPENDIX H: OBSERVATION OF *DICTYOSTELIUM DISCOIDEUM* AGGREGATION

The *D. discoideum* Ax4 cell line carrying the plasma membrane marker PKBR1(N150)-mScarlet-I-2x at the *act5* locus [85] was used. The cell culture, development, microfabrication, and observation were performed as described previously [83,85]. To image a monolayer cell population [Fig. 7(a)], cells dissociated from the slugs were suspended at a density of 2.2×10^5 cells/mL in phosphate buffer (PB: 12 mM KH_2PO_4, 8 mM Na_2HPO_4, pH 6.5). To observe the translational motion and rotational motion of two cells [Figs. 7(e) and 7(f)], cells were suspended at a density of 5×10^4 cells/mL in PB with [Fig. 7(f)] or without [Fig. 7(e)] 100 μM SQ22536 (Wako). Then, 0.4 mL of cell suspension was loaded into a microfluidic chamber with a height of 2.5 [Fig. 7(a)] or 4 [Figs. 7(e) and 7(f)] μm. Fluorescence images were acquired at 22°C using an inverted microscope (IX83, Olympus/Evident) equipped with a multibeam confocal scanning unit (CSU-W1, Yokogawa) and CMOS cameras (ORCA-FusionBT, Hamamatsu Photonics).

The membrane images of *D. discoideum* were collected at 5-second intervals to obtain $I = 361$ frames [Fig. 7(a)]. The raw images were binarized using Trainable Weka Segmentation in Fiji, and cells were detected by connected component labeling. Hereafter, cells are represented by their centroid positions. A pair of cells in consecutive frames was identified as the same cell if the opponent had the smallest distance among other cells in the same frame. In this way, we obtained $N_\mathrm{c} = 507$ trajectories $\{\boldsymbol{r}_\alpha(i)\}_{\alpha=1,\cdots,N_\mathrm{c},i=1,\cdots,I}$, which include more than 100 frames. Note that some cells were occasionally not detected so that a true trajectory with full length could be divided into multiple trajectories with shorter lengths. Then, cells were assigned velocity vectors $\{\boldsymbol{v}_\alpha(i)\}$ at each time point. We applied a mean filter with a length of 10 frames before taking the difference between consecutive centroid positions to remove the noise. For the antiparallel circulation pattern analysis, the circulation velocity was calculated at each time point i (see Appendix D).

To investigate the frequency of the reversal movement of the cells, we calculated the persistent time of the circulation direction. Using the autocorrelation coefficient

$$\rho_\alpha(j) = \sum_i \mathrm{sgn}\, v_\alpha^{\mathrm{circ}}(i) \mathrm{sgn}\, v_\alpha^{\mathrm{circ}}(i+j), \tag{22}$$

the persistent time τ_α is defined as the first zero-crossing point, i.e.,

$$\tau_\alpha = 5\min\{\, j \mid \rho_\alpha(j) \leq 0\}. \tag{23}$$

When $\rho_\alpha(j) > 0$ for all J, the persistent time is longer than or equal to the length of the trajectory.

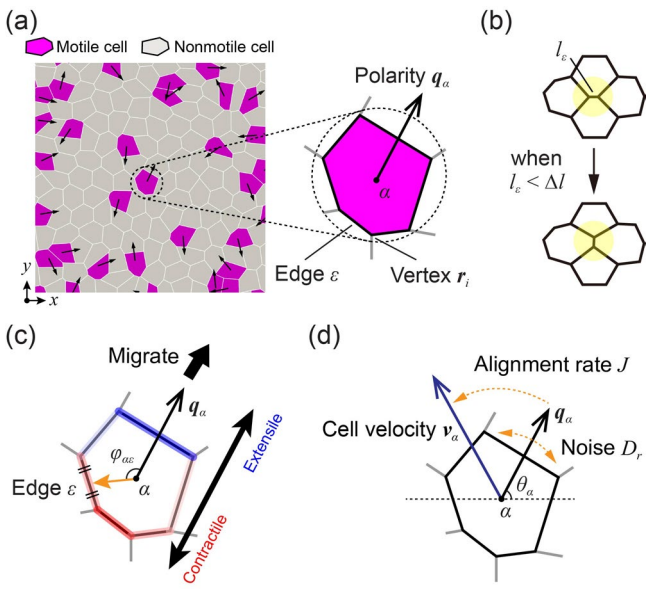

FIG. 1. Setup of the model. (a) The system is represented by a polygonal tiling with periodic boundary conditions. Each polygon expresses the shape of an individual cell. Purple and gray polygons represent motile-type and nonmotile-type cells, respectively. Arrows indicate polarity vectors of the motile-type cells. (b) Schematic illustration of a T1 transition. When the edge length l_ε becomes shorter than Δl, the cell configuration is rearranged by reconnecting the network of vertices and edges. (c) Tension gradient generated within a motile-type cell at its boundary with adjacent cells. Relative to the polarity vector, negative tension at the leading edge causes the edge to extend, and positive tension contracts the rear edge, causing contraction. (d) Schematic illustration of self-alignment. Each polarity vector tends to align with the velocity of the cell centroid with an alignment rate J and undergoes rotational diffusion with noise intensity D_r.

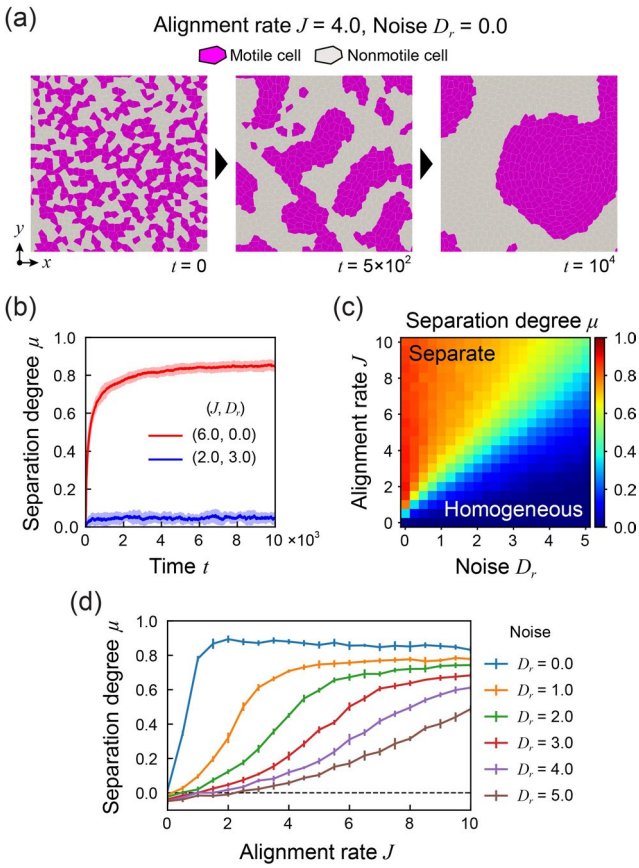

FIG. 2. Phase separation of the system. (a) Time evolution of the system with an alignment rate of $J = 4.0$ and a noise intensity of $D_r = 0.0$ (also shown in Movie S1). Purple and gray polygons represent motile-type and nonmotile-type cells, respectively. Starting from a homogeneous initial state at $t = 0$, motile-type cells spontaneously aggregate, leading to phase separation. (b) Time evolution of the separation degree μ for two parameter sets: $(J, D_r) = (6.0, 0.0)$ and $(J, D_r) = (2.0, 3.0)$. The line and band widths in the plot indicate the statistical average values and standard deviations, respectively. (c) Phase diagram of the separation degree μ as a function of J and D_r. (d) Separation degree μ as a function of J with $D_r = \{1.0, 2.0, 3.0, 4.0, 5.0\}$.

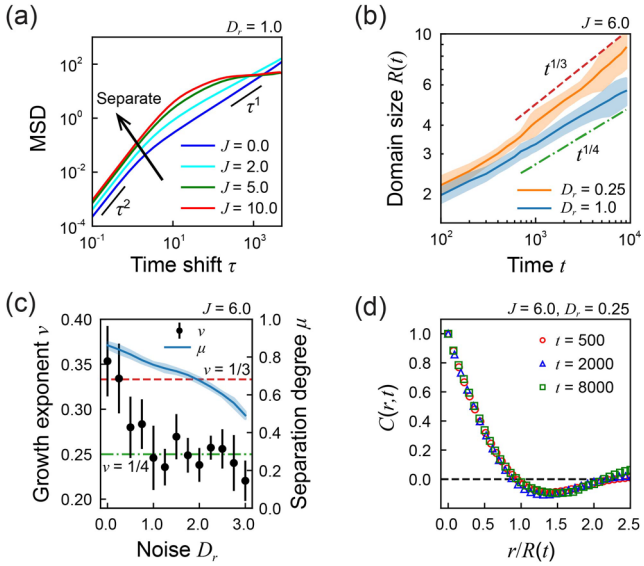

FIG. 3. Macroscopic behavior of motile-type cells and domains. (a) Mean-square displacement (MSD) of motile-type cells as a function of the time shift τ. (b) Time evolution of the domain size R with $J = 6.0$ for $D_r = 0.25$ and $D_r = 1.0$. The line and band widths in the plot indicate the statistical average values and standard deviations, respectively. (c) Growth exponent ν (black point) and separation degree μ (blue line) as a function of noise intensity D_r with $J = 6.0$. (d) Spatial correlation function of cell types $C(r,t)$ as a function of the distance between cells r, normalized by the domain size R, with $(J, D_r) = (6.0, 0.25)$.

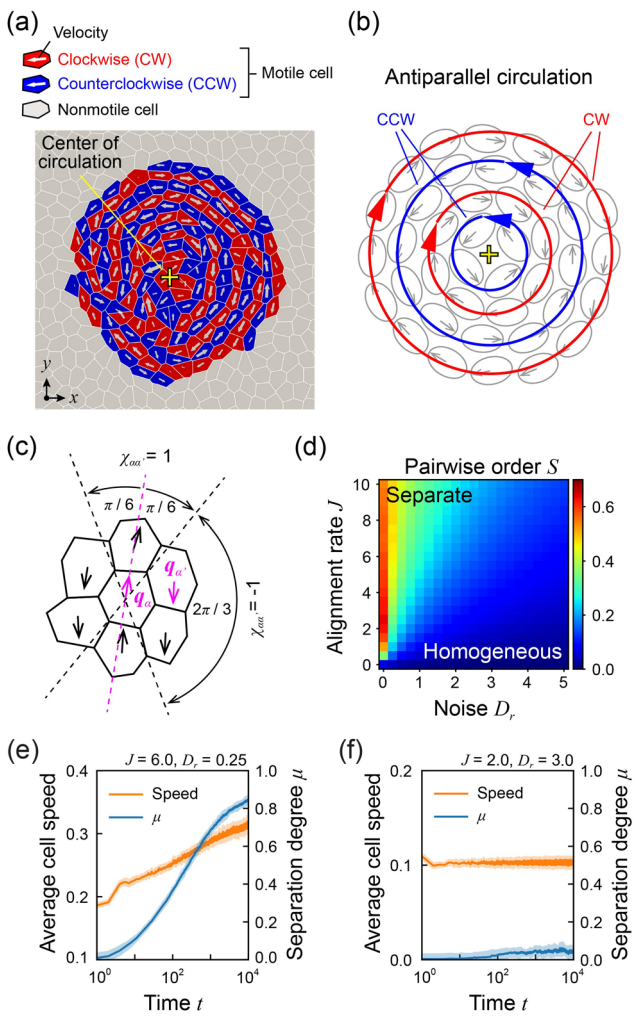

FIG. 4. Antiparallel circulation within a motile-type cell domain. (a) Snapshot of a motile-type cell domain with $(J, D_r) = (5.0, 0.0)$ at $t = 108$ (also shown in Movie S3). Motile-type cells rotating clockwise (CW) around the center of circulation are colored red, and those rotating counterclockwise (CCW) are colored blue. Nonmotile-type cells are colored gray. White arrows indicate cell velocities. (b) Schematic illustration of antiparallel cell circulation within a motile-type cell domain. Red arrows represent CW trajectories, and blue arrows represent CCW ones. The circulations are concentrically aligned, with adjacent layers moving in antiparallel directions. (c) Schematic definition of the weight $\chi_{\alpha\alpha'}$ for calculating the pairwise order parameter S. If the center of the α'-th cell, adjacent to the α-th cell, lies within the sector ranging from $\pi/3$ forward or $\pi/3$ backward relative to the polarity vector $\boldsymbol{q}_\alpha$ of the α-th cell, then $\chi_{\alpha\alpha'} = 1$; otherwise, $\chi_{\alpha\alpha'} = -1$. (d) Phase diagram of the pairwise order S as a function of J and D_r. (e, f) Average speed of motile-type cells (orange line) and separation degree μ (blue line) as a function of time t with $(J, D_r) = (6.0, 0.25)$ (e) and $(J, D_r) = (2.0, 3.0)$ (f).

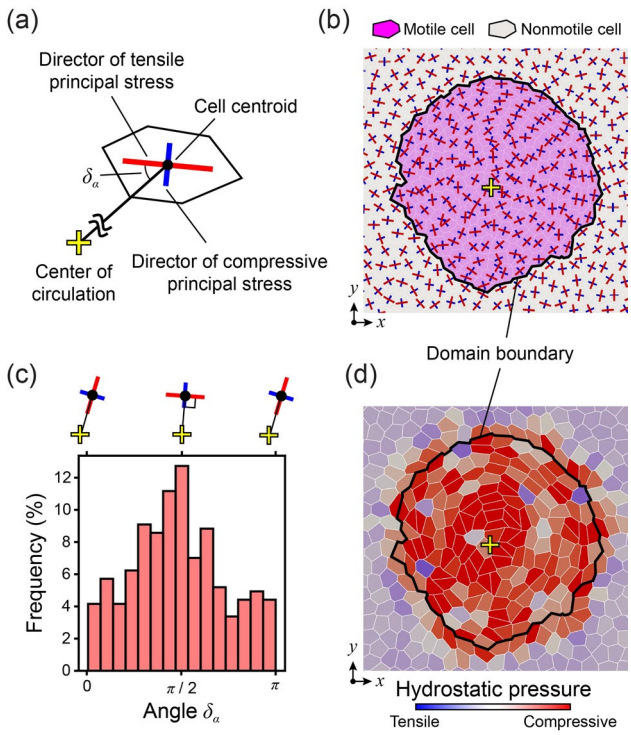

FIG. 5. Stress distribution and orientation around a domain. (a) Schematic illustration of the principal stress directions: the red line represents the director of tensile principal stress, and the blue line represents that of compressive principal stress. The angle δ_α is defined as the angle between the tensile principal stress direction and the line segment from the center of circulation to the cell centroid. The domain center is marked by a cross. (b) Stress directors for each cell. Motile-type and nonmotile-type cells are colored purple and gray, respectively. (c) Distribution of the directors of tensile principal stress for individual cells. (d) Hydrostatic pressure in each cell. In (b) and (d), the black line indicates the boundary between motile-type and nonmotile-type cell regions.

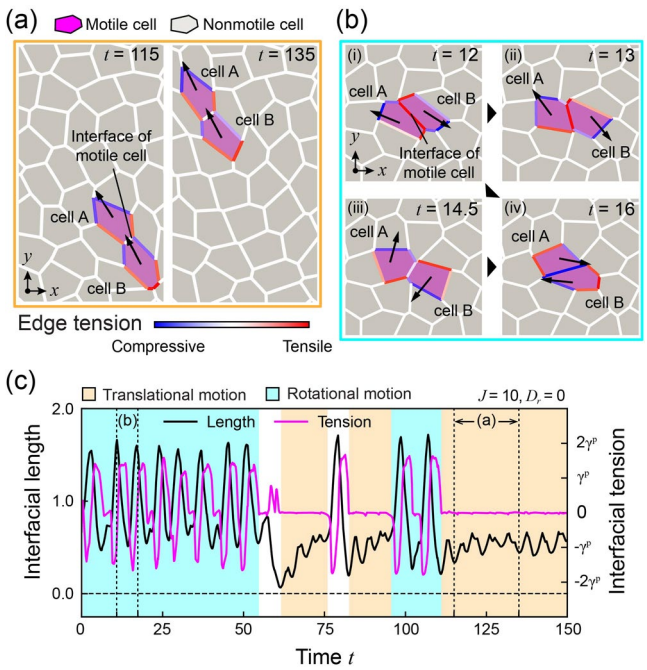

FIG. 6. Pairwise cell motion driven by self-alignment. (a, b) Snapshots of a motile-type cell pair in translational motion (a) and rotational motion (b) (also shown in Movie S4). Motile-type and nonmotile-type cells are colored purple and gray, respectively. Arrows indicate the polarity vectors of the motile-type cells. Edge colors indicate the intensity of edge tension. (c) Time evolution of the interfacial edge length (black) and edge tension (purple) for a motile-type cell pair with $(J, D_r) = (10, 0.0)$. The orange and purple regions indicate the time intervals when the cell pair is in translational and rotational motion, respectively. Snapshots (a) and (b) correspond to the time points within the intervals marked by dashed lines in (c).

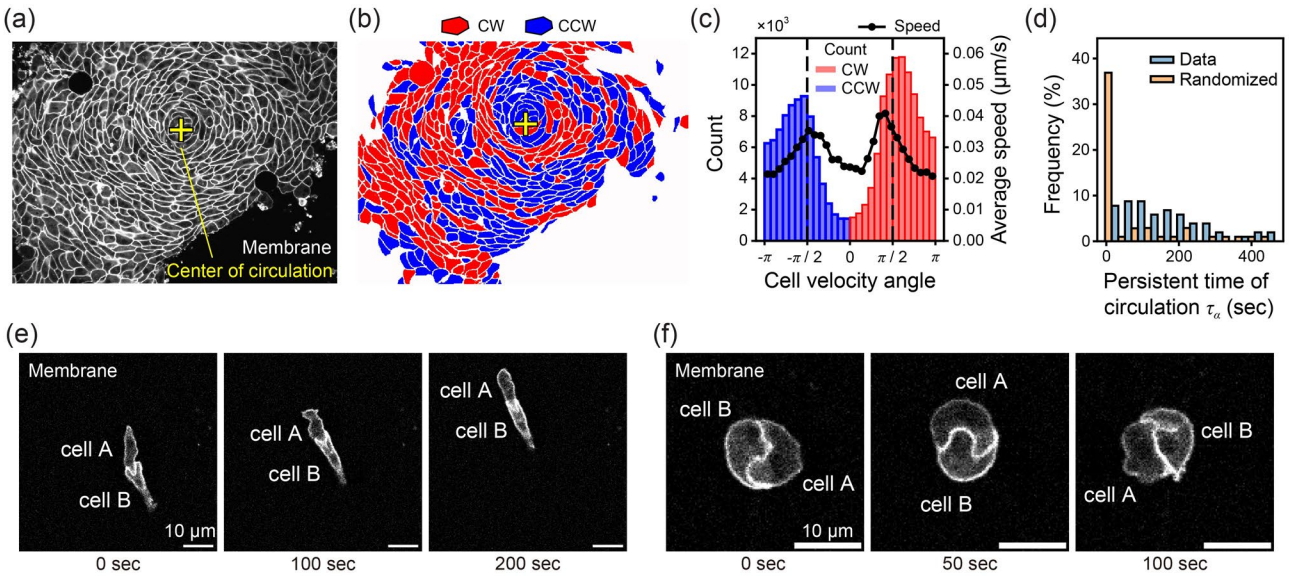

FIG. 7. Antiparallel circulation and pairwise motion of *Dictyostelium discoideum* cells. (a) A snapshot of a *D. discoideum* aggregate in a 2D chamber. (b) Circulation directions of cells around the center (also shown in Movie S5). Cells exhibiting clockwise (CW) circulation are colored red, and those with counterclockwise (CCW) circulation are colored blue. In panels (a) and (b), the yellow cross marks the center of circulation. (c) Distribution of cell migration directions (CW: red; CCW: blue) and average cell speed (black line) as a function of angle. The angle is defined between the direction of cell migration and the vector from the domain center to the center of circulation. (d) Distribution of the circulation persistent time τ_α for the raw data (blue) and randomized data generated via bootstrap sampling (orange). (e, f) Snapshots of a two-cell cluster showing head-to-tail translational motion (e) and rotational motion (f). In panels (a), (b), (e), and (f), cell boundaries are shown in white.

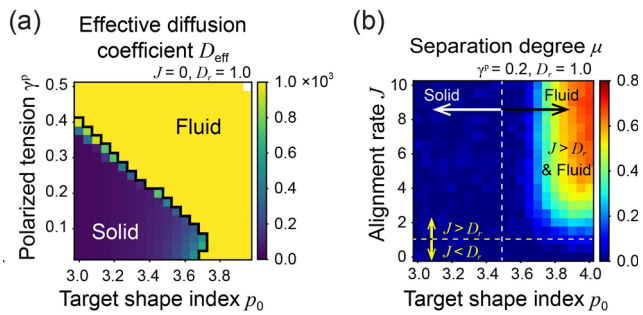

FIG. 8. Jamming transition of the system. (a) Phase diagram of the effective diffusion coefficient D_{eff} as a function of the target shape index p_0 and strength of polarized tension γ^{p} with $(J, D_r) = (0.0, 1.0)$. (b) Phase diagram of the separation degree μ as a function of p_0 and J with $\gamma^{\mathrm{p}} = 0.2$ and $D_r = 1.0$. The white dotted line indicates the target shape index threshold, which determines whether the tissue is in a solid-like state or fluid-like state. The yellow dotted line indicates the alignment rate at which the value is equal to the noise.

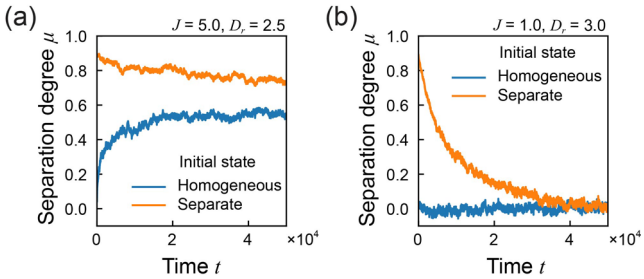

FIG. 9. Dependence of phase separation on initial conditions. (a, b) Time evolution of the separation degree μ with $(J, D_r) = (5.0, 2.5)$ (a) and $(J, D_r) = (1.0, 3.0)$ (b). In panels (a) and (b), the blue and orange lines indicate the case with a homogeneous initial state and the case with a separated initial state, respectively.

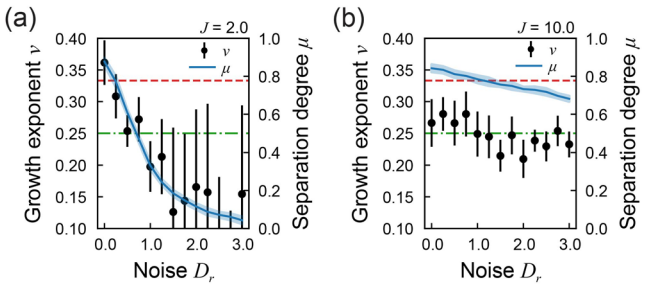

FIG. 10. Dependence of the domain growth exponent on the alignment rate and noise. (a, b) The growth exponent ν and separation degree μ as a function of noise intensity D_r with $J = 2.0$ (a) and $J = 10.0$ (b). The red dashed line and green dash-dotted line indicate $\nu = 1/3$ and $\nu = 1/4$, respectively.

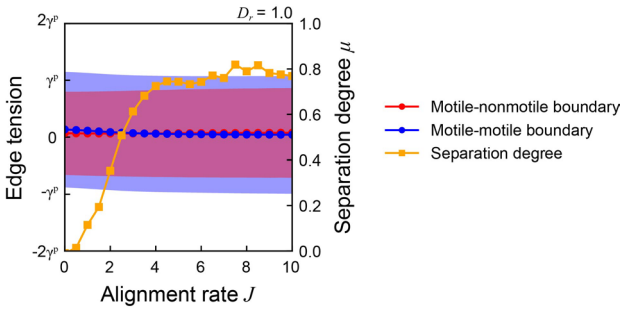

FIG. 11. Exerted tension at the boundary between motile-type and nonmotile-type cells. The tension between motile-type and nonmotile-type cells (red), tension between motile-type cells (blue), and separation degree μ (yellow) are plotted as a function of J with $D_r = 1.0$. The lines represent average values, and the band widths represent standard deviations.